

Programmable k -local Ising Machines and all-optical Kolmogorov-Arnold Networks on Photonic Platforms

Nikita Stroeve¹ and Natalia G. Berloff^{2,*}

¹*Department of Physics of Complex Systems, Weizmann Institute of Science, Rehovot 76100, Israel*

²*Department of Applied Mathematics and Theoretical Physics, University of Cambridge, UK*

(Dated: August 26, 2025)

We unify k -local Ising optimization and optical KAN function learning on a single photonic platform, establishing a critical convergence point in optical computing that enables interleaved discrete-continuous workflows. We introduce a single spacial light modulator (SLM)-centric primitive that realizes, in one stroke, all-optical k -local Ising interactions and fully optical Kolmogorov-Arnold network (KAN) layers. The central idea is to convert structural nonlinearity of a nominally linear photonic scatterer into a per-window computational resource by adding one relay pass through the same spatial light modulator. A folded 4f relay reimages the first Fourier plane onto the SLM so that each chosen spin clique or ridge channel occupies a disjoint window with its own second-pass phase patch. Propagation remains linear in the optical field, yet the measured intensity in each window becomes a freely programmable polynomial of the clique sum or projection amplitude. This yields native, per-clique k -local couplings without nonlinear media and, in parallel, the many independent univariate nonlinearities required by KAN layers, all with in-situ physical gradients for training using two-frame (forward and adjoint) physical gradients. We outline implementation on spatial photonic Ising machines, injection-locked VCSEL arrays, and the Microsoft analog optical computers. In all cases the hardware change is one extra lens and a fold (or an on-chip 4f loop), enabling a minimal overhead, massively parallel route to high-order optical Ising optimization and trainable, all-optical KAN processing.

I. INTRODUCTION

Ising machines are physical simulators that seek low-energy configurations of an Ising-type cost function by exploiting analog optical, electronic, or quantum dynamics. They have emerged as high-throughput engines for quadratic unconstrained binary optimization (QUBO) and for sampling from near-Boltzmann distributions [1]. Realizations now include free-space SLM-based photonic Ising machines, polaritonic and photonic Ising machines, large-scale coherent Ising machines and integrated DOPO networks, as well as electronic annealers and Ising-inspired engines (simulated bifurcation, analog iterative machines) and spintronic p-bit computers; see, e.g., [2–15]. Optical realizations are particularly attractive because diffraction and interference deliver native, reconfigurable all-to-all linear coupling with negligible latency and excellent parallelism; in free-space spatial-photonic systems millions of spins can be encoded on a single spatial light modulator (SLM) aperture [8], while injection-locked vertical-cavity surface-emitting laser (VCSEL) arrays achieve sub-nanosecond state updates at rack-scale densities [16]. These attributes make optics a natural substrate for both native k -local interactions and for the per-ridge nonlinearities required by Kolmogorov-Arnold networks (KANs), motivating the unified approach developed below.

Despite this breadth, most deployed platforms are intrinsically quadratic. A 2-local Ising Hamiltonian with

binary spins $s_i \in \{\pm 1\}$ reads

$$H_{2\text{-local}} = \sum_i h_i s_i + \sum_{i < j} J_{ij} s_i s_j, \quad (1)$$

where h_i are local bias (field) terms acting on individual spins, J_{ij} are symmetric coupling coefficients between spins i and j , and $\sum_{i < j}$ denotes a sum over all distinct unordered spin pairs. Many practically important formulations are k -local with $k > 2$, including clauses in k -SAT and related constraint-satisfaction problems, parity-check constraints in coding theory, and multi-spin interactions in statistical and condensed-matter models such as Ising lattice gauge theories and topological stabilizer codes; see, e.g., [17–22]. Any k -local polynomial can be reduced to quadratic form by introducing auxiliary (ancilla) variables and penalty couplings, a process known as quadratization [23]. However, this transformation comes at a cost: the number of variables increases, and the additional constraints broaden the coupling distribution and complicate the energy landscape, often making the resulting quadratic instances empirically harder to solve than the original higher-order ones [24]. In practice this means more spins, wider dynamic ranges for J_{ij} , and more rugged energy surfaces; all of which degrade optical and electronic heuristics and annealers. Recent work has demonstrated that direct k -local implementations can achieve 3 orders of magnitude reduction in required variables compared to quadratization approaches [25, 26], motivating the development of native k -local hardware.

A complementary algorithmic direction shows why such hardware is valuable. Exact spin-elimination tech-

niques remove variables from an Ising Hamiltonian while preserving the ground state by absorbing their effects into higher-order couplers among remaining spins [27]. This trades dimensionality for locality: large quadratic instances compress into fewer spins with multi-spin links. In other words, eliminating a spin is equivalent to creating a higher-order term on its neighbors; having native k -local hardware makes this transformation a feature rather than a burden. Consequently, algorithmic preprocessing and native k -local optics are aligned: the former produces multi-spin links that the latter can represent directly.

Beyond combinatorial optimization, there is growing demand for analog photonic processors that support nontrivial machine-learning primitives. A Kolmogorov-Arnold Network (KAN) implements a function $f: \mathbb{R}^n \rightarrow \mathbb{R}$ as

$$f(x_1, \dots, x_n) = \sum_{j=1}^{2n+1} \Phi_j \left(\sum_{i=1}^n \phi_{i,j}(x_i) \right), \quad (2)$$

where $x_i \in \mathbb{R}$ are the input variables, $\phi_{i,j}(\cdot)$ are trainable univariate functions applied to each input, $\Phi_j(\cdot)$ are trainable outer univariate functions that combine the inner sums, the sum over $j = 1, \dots, 2n + 1$ follows the Kolmogorov-Arnold theorem, which guarantees that any continuous multivariate function can be represented in this form [28]. For optical platforms, we adopt the shallow variant of the KAN architecture and will use slightly different format: a multivariate mapping $F: \mathbb{R}^d \rightarrow \mathbb{R}$ as a finite sum of learnable univariate functions acting on linear projections,

$$F(x) = \sum_{m=1}^M \Phi_m(w_m^\top x), \quad (3)$$

with projection vectors w_m and ridge functions Φ_m trained jointly [29].

KAN-type architectures have universal-approximation guarantees (e.g., P1-KAN; KKANs). Formal comparisons proving a global, orders-of-magnitude parameter reduction over multilayer perceptrons (MLP) for universal approximation do not exist to our knowledge. Empirically, there are tasks (e.g., Poisson PDE) where a small KAN matches or exceeds the accuracy of a much larger MLP with roughly $100\times$ fewer parameters [29]. The first photonic KAN implementation demonstrated $65\times$ reduction in energy consumption and $50\times$ improvement in latency compared to traditional photonic neural networks, validating the potential for optical KAN realizations [30]. KANs have been deployed commercially for credit-risk modeling and fraud detection [31]. Equation (3) is natural for optical implementation: the projections are realized by beam-splitting or diffraction, and each Φ_m is an independent, univariate nonlinearity. Critically, an all-optical KAN therefore requires many independent, per-ridge, programmable univariate nonlinearities. With this

context, we now summarize the operational status and problem reach of the three optical lines of attack most relevant to this work.

Spatial-photonic Ising machines (SPIMs) encode spins in the phase of an SLM and realize pairwise couplings through free-space diffraction and programmable phase redistribution [8, 32]. Recent advances have achieved full programmability through focal plane division [33, 34] and monolithic integration with sub-microsecond operation times [35]. Their strengths are flexible reprogrammability of J_{ij} , effectively dense connectivity inherited from Fourier optics, and massive spatial parallelism. SPIMs excel on quadratic problems such as Max-Cut, graph partitioning, community detection, and Ising inference, and they can operate in sampling modes by leveraging noise and gain control. In current form, however, the optical nonlinearity is either global or delegated to electronic thresholding; independently weighted k -body interactions and the many per-ridge nonlinearities needed in optimization or for a KAN realization are not available within the optical loop.

Injection-locked VCSEL arrays map spins to orthogonal linear polarizations of mutually coupled lasers and deliver nanosecond-scale state updates with electronically tunable pairwise couplings [16]. Injection locking ensures mutual coherence and polarization control across the array, enabling precise, high-rate optical feedback. These arrays offer genuine oscillator dynamics, compact footprints, and electronic addressability of coupling graphs. They are effective for fast heuristics and sampling on 2-local QUBO instances and for real-time, event-driven optimization. Presently, multi-spin terms are not natively programmable in the optical feedback path, and there is no provision for the hundreds of independent per-ridge optical nonlinearities required by KANs.

Microsoft’s analog optical computer (AOC) performs the matrix-vector multiplication in optics and realizes all remaining primitives of the fixed-point iteration in analog electronics [12]. The state $s_t \in \mathbb{R}^N$ at time t is encoded as intensities of a micro light-emitting diode (microLED) array and multiplied optically by an SLM that stores the weight matrix $W \in \mathbb{R}^{N \times N}$. Three-dimensional (3D) fan-in/fan-out free-space optics distribute light from each microLED across an SLM row for element-wise modulation, and the signals are summed column-wise on a photodetector (PD) array to produce the optical matrix-vector product (by optical vector-matrix multiplication, OVMM). Signed weights are implemented by loading the positive and negative parts of W onto two SLMs and combining the corresponding PD outputs by differential analog readout. The resulting channel voltages undergo an element-wise analog nonlinearity $f: \mathbb{R}^N \rightarrow \mathbb{R}^N$ and configurable per-channel gains that implement an annealing schedule $\alpha(t) \in \mathbb{R}$ and a momentum coefficient $\gamma \in \mathbb{R}$. One discrete iteration (corresponding to a single opti-

cal-electronic round trip) is

$$s_{t+1} = \alpha(t)s_t + Wf(s_t) + \gamma(s_t - s_{t-1}) + b, \quad (4)$$

where $b \in \mathbb{R}^N$ is a programmable bias vector. This combination of 3D fan-in/fan-out OVMM with per-channel analog processing supports fixed-point inference for equilibrium-style machine-learning models and combinatorial optimization (e.g., quadratic unconstrained mixed optimization and Ising formulations) within the unified AOC abstraction. In the current instantiation, f is implemented electronically and its functional form is shared across channels; native optical k -local interactions within a clique and independently programmable optical nonlinear “ridge” functions per channel are not supported by this hardware.

Across these platforms the same limitation recurs. They excel on 2-local Hamiltonians and iterative quadratic programs, but native, per-clique k -local interactions and the many independent, trainable univariate nonlinearities required by KANs are not yet supported in optics. Prior optical demonstrations of high-order terms have relied on explicit material nonlinearities such as $\chi^{(2)}$ and Kerr/parametric processes, which add alignment-critical components, raise power budgets, and hard-wire interaction topologies [36, 37]. This motivates a creating of a single, platform-agnostic optical primitive that supplies both capabilities simultaneously.

Recent work shows that large, trainable effective nonlinearities do not require material $\chi^{(2)}$ or $\chi^{(3)}$ media [38]. Large-scale nonlinear photonic computing with over 27,000 input nodes using structural nonlinearity in disordered networks was demonstrated [39], while sub-nanosecond nonlinear operations in integrated photonic processors was also achieved [40]. In a linear, time-invariant photonic circuit driven by a monochromatic input $a_{\text{in}}(\omega)$, the output $a_{\text{out}}(\omega; \theta) = S(\omega, \theta)a_{\text{in}}(\omega)$ depends nonlinearly on the programmable phases θ because the steady-state scattering operator enters through a resolvent,

$$S(\omega, \theta) = -i\sqrt{\kappa}[\omega - H(\theta)]^{-1}\sqrt{\kappa}, \quad (5)$$

where $\kappa \succeq 0$ collects the coupling rates between internal modes and external ports, and $H(\theta)$ is the effective non-Hermitian Hamiltonian governing the internal linear network (detunings, losses, and couplings). The measured intensities $I(\theta) = |a_{\text{out}}|^2$ are nonpolynomial in θ . For any scalar loss $\mathcal{L}(I(\theta), I_{\text{tgt}})$, the gradient $\partial\mathcal{L}/\partial\theta$ is obtained exactly from two optical frames: a forward pass with a_{in} and an adjoint pass that injects a source proportional to $\partial\mathcal{L}/\partial a_{\text{out}}^*$ at the outputs; combining the two camera measurements yields $\partial\mathcal{L}/\partial\theta$ without electronic backpropagation [38]. We adopt this two-frame adjoint protocol as the default hardware method; when we report software-only tests, we emulate it with an forward-differences proxy (two evaluations per parameter), while

noting that the hardware requires only two frames per update.

In a similar spirit, Yildirim et al. exploited this structural nonlinearity in a multi-bounce free-space architecture (nPOLO), using repeated SLM bounces to emulate activation functions for image classification without any nonlinear crystal [41]. Unlike these demonstrations, which either act on a single global optical mode [38] or impose one polynomial shared across the entire SLM aperture [41], our two-pass relay method introduced below makes structural nonlinearity local and addressable. Each disjoint Fourier-plane window (clique or ridge) carries its own independently trained polynomial response, enabling massively parallel, per-clique k -local Ising couplings and the many per-ridge nonlinearities required for a fully optical KAN within the same optical loop.

This paper therefore addresses two outstanding challenges within a single optical framework. First, all-optical implementation of programmable k -local Ising couplings: can structural nonlinearity alone deliver independently weighted, clique-specific k -body interactions on SPIM, VCSEL, or AOC hardware, eliminating additional nonlinear optics? Second, all-optical KAN implementation: can the same mechanism supply hundreds of independent, trainable univariate functions, enabling a gradient-trainable photonic KAN?

We answer both questions affirmatively by introducing a two-bounce relay that re-images the first Fourier plane back onto the SLM (or onto a programmable saturable absorber in a VCSEL feedback loop). The second programmable phase mask acts on the summed spin field of each selected clique; through the structural inverse, the detected intensity realizes an arbitrary univariate polynomial that can be optimized with the physical gradients of Ref. [38]. Because every k -spin product depends only on this sum, our scheme embeds fully programmable k -local weights without $\chi^{(2)}$ or Kerr elements, while simultaneously providing the independent ridge functions required for a KAN. As shown in Sec. II, a parity-matched harmonic basis on the second pass implies a minimal parameter count $M(k) = \lceil k/2 \rceil$ trainable mask depths per clique window; closed-form seeds and two-frame, in-situ physical gradients complete calibration. The hardware changes relative to a pairwise SPIM are minimal: one additional lens and a folding mirror (or an on-chip $4f$ loop).

Our paper is arranged as follows. We formulate the proposal of the mapping from k -body Ising terms to learnable polynomials of summed spin amplitudes in Section II, where we formalize the optical representation and learning of k -local cliques (parity-matched univariate polynomials of the clique sum, the two-bounce relay, calibration and learning rule), including a worked $k = 4$ example and numerical calibration/refinement benchmarks. In Section III we repurpose the same primitive to implement all-optical Kolmogorov-

Arnold network (KAN) layers on SPIMs and outline a multi-bounce (nPOLO) variant, together with simulated in-situ-gradient training. Throughout, “two-frame physical gradients” refers to the adjoint protocol that measures all parameter gradients from two optical frames per update (forward + adjoint) without electronic back-propagation. In Sec. III we emulate this hardware protocol in software by a finite-difference proxy (FD proxy) that requires two evaluations per parameter; we label results accordingly. The hardware frame count remains two per update. Section IV details programmability on injection-locked VCSEL arrays and on the analog optical computer (AOC). Section V concludes with scalability, engineering considerations, and outlook.

Our results elevate structural nonlinearity from a single global activation to a massively parallel, per-clique resource, establishing a hardware-minimal path toward high-order optical Ising optimization and gradient-trained photonic KAN processors.

II. OPTICAL REPRESENTATION AND LEARNING OF k -LOCAL CLIQUES

The purpose of this section is to describe, in operational detail, how the two-bounce architecture introduces k -local terms into the physically measured energy of the machine, and how the corresponding per-clique parameters are learned from optical data. We begin by stating the target energy and its optical surrogate, then explain how the relay isolates clique sums, give an explicit $k = 4$ example, and conclude with the learning rule and numerical simulations of the training dynamics. Our approach builds on recent advances in programmable spatial-photonic systems [32, 33] while addressing the critical need for native k -local implementations identified by recent optimization studies [25, 26, 42].

From a k -local target to a measured optical surrogate. Let $s_i \in \{\pm 1\}$ denote N binary spins. A k -local Ising Hamiltonian is any energy function that can be written as a sum of interaction terms of order at most k ,

$$H_{\leq K}(s) = \sum_{k=1}^K \sum_{\substack{q \subseteq \{1, \dots, N\} \\ |q|=k}} J_q^{(k)} \prod_{i \in q} s_i, \quad (6)$$

where $J_q^{(k)}$ is the coupling assigned to the subset q of size $|q| = k$. The case $k = 1$ gives on-site fields, $k = 2$ gives pairwise couplings, and $k \geq 3$ gives genuine multi-spin interactions.

We fix an order k , let $C_k = \{q \subseteq \{1, \dots, N\} : |q| = k\}$ be the family of k -spin cliques and write the k -local target contribution as

$$E_k^{\text{target}}(s) = \sum_{q \in C_k} J_q \prod_{i \in q} s_i. \quad (7)$$

Within each clique the product is permutation-symmetric and depends only on the clique sum

$$S_q = \sum_{i \in q} s_i \in \mathcal{S}_k, \quad \mathcal{S}_k = \{-k, -k+2, \dots, k-2, k\}. \quad (8)$$

By one-dimensional interpolation on the discrete set \mathcal{S}_k with the parity constraint implied by k , there exists a unique univariate polynomial of degree at most k and with the same parity as k such that [43, 44]

$$\prod_{i \in q} s_i = \Phi_q(S_q), \quad \Phi_q(S_q) = \sum_{\substack{r=0 \\ r \equiv k \pmod{2}}}^k c_{r,q} S_q^r, \quad (9)$$

where Φ_q is the clique polynomial and $c_{r,q} \in \mathbb{R}$ are its coefficients, nonzero only for exponents r with the same parity as k .

For instance, take $k = 4$, $q = \{i, j, l, m\}$, so that the clique we want to represent is $\prod_{i \in q} s_i = s_i s_j s_l s_m$. The clique sum is $S_q = s_i + s_j + s_l + s_m$, so that $S_q \in \{-4, -2, 0, 2, 4\}$ and the product $\prod_{i \in q} s_i$ equals $+1$ for $S_q \in \{-4, 0, 4\}$ and -1 for $S_q \in \{-2, 2\}$. The unique univariate polynomial that represents the clique is $\Phi_q(S_q) = S_q^4/24 - 2S_q^2/3 + 1$, so is given by Eq. (9) with $c_{0,q} = 1, c_{2,q} = -2/3, c_{4,q} = 1/24$.

The optical measurement associated with clique q is defined as follows. For an input proportional to a prescribed scalar S_q delivered to the window of clique q by the first pass, and for a second-pass phase patch parameterised by vector θ_q (i.e., the dedicated sub-aperture of the SLM hit by the return image of window q , on which we program a small-depth, y -periodic phase profile), the camera records a window-integrated intensity $I_q(S; \theta_q) \in \mathbb{R}$. The machine’s measured k -local energy is then

$$E_k^{\text{meas}}(s; \theta_q) = \sum_{q \in C_k} w_q I_q(S_q; \theta_q) + \text{const}, \quad (10)$$

with w_q a per-clique scalar gain and const an s -independent additive offset. By symmetry and for small phase depths on the second pass, the window-averaged intensity admits an even- or odd-parity polynomial expansion in S_q ,

$$I_q(S_q; \theta_q) = \sum_{\substack{r=0 \\ r \equiv k \pmod{2}}}^k \Gamma_{r,q}(\theta_q) S_q^r, \quad (11)$$

where $\Gamma_{r,q}$ are smooth functions of the phase-patch parameters determined by the relay geometry and the chosen basis on the second pass: $w_q \Gamma_{r,q} = J_q c_{r,q}$, for all parity-matched r . The constant $\Gamma_{0,q}$ contributes only a global energy offset and can be ignored when matching to E_k^{target} .

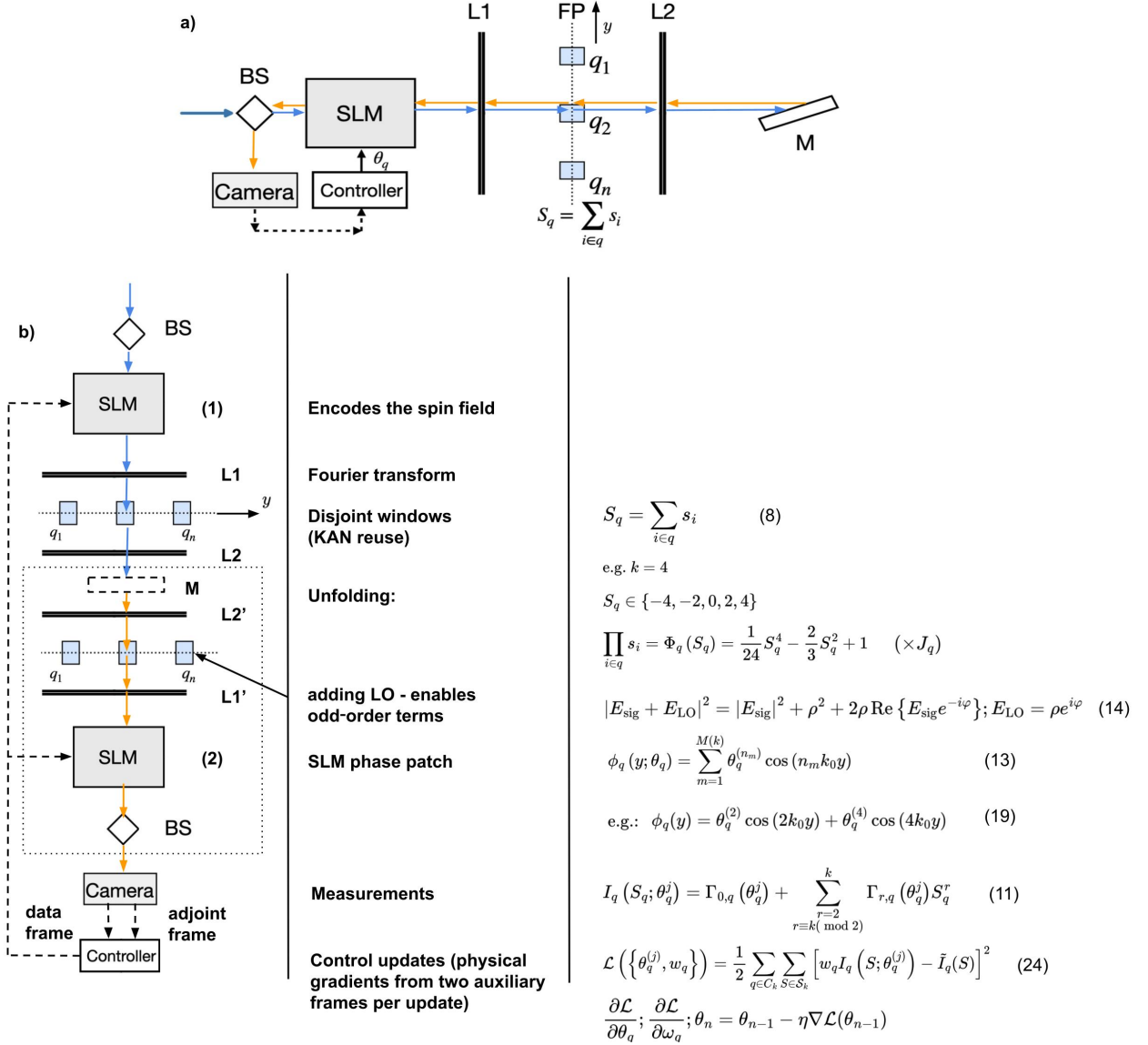


FIG. 1. **Folded 4f relay for per-clique structural nonlinearity and in-situ training.** (a) The spatial-light modulator (SLM) encodes the spin field on the first pass. Lens L_1 performs a Fourier transform; in the Fourier plane (dotted line) disjoint windows q isolate the summed spin $S_q = \sum_{i \in q} s_i$. Lens L_2 re-images this plane back onto the same SLM for a second programmable phase pass, where an independent patch $\phi_q(y; \theta_q)$ acts only on S_q (with y the in-patch coordinate). A beam splitter (BS) directs the return beam to a camera; frames are streamed to the controller (dashed arrow), which computes per-window intensities I_q , obtains two-frame physical gradients, and updates θ_q on the SLM (solid arrow), closing the loop. M denotes the folding mirror. Blue/orange paths denote the first/return optical passes. *Mnemonic:* L_1 collects spin contributions into sums S_q in separate Fourier-plane windows; L_2 sends those windows back onto separate patches of the same SLM, where small-depth, parity-matched cosine gratings shape a per-window polynomial response. On the first pass, each spin macropixel carries a multi-tone, phase-only micro-grating that fans out that spin's light to every window that needs it. (b) Conceptual unfolded view of the same relay. The dashed box marks the backward (return) pass (orange). The middle column lists the actions of each stage; the right column annotates the relations used in the text: S_q (Eq. 8); a parity-matched second-pass basis $\phi_q(y) = \phi_q(y; \theta_q)$ (Eqs. 13,19) yielding a window-averaged response $I_q = \Gamma_{0,q} + \sum_{r \equiv k \pmod{2}} \Gamma_{r,q} S_q^r$ (Eq. 11); an optional weak local oscillator enabling odd orders (Eq. 14); and per-clique fitting of $\{\theta_q, w_q\}$ by minimizing the quadratic loss (Eq. 24). In the folded layout, $\text{SLM}(1) = \text{SLM}(2)$ and $L'_1 = L_1$, $L'_2 = L_2$; primes denote the return pass in the conceptual unfolding.

Local coefficient map and its Jacobian. For window q we collect the non-constant, parity-matched coefficients into the vector

$$\Gamma_q(\theta_q) \equiv \begin{bmatrix} \Gamma_{k,q}(\theta_q) \\ \Gamma_{k-2,q}(\theta_q) \\ \vdots \\ \Gamma_{r_{\min},q}(\theta_q) \end{bmatrix}, \quad \theta_q \equiv \begin{bmatrix} \theta_q^{(n_{M(k)})} \\ \theta_q^{(n_{M(k)-1})} \\ \vdots \\ \theta_q^{(n_1)} \end{bmatrix},$$

where $r_{\min} = 2$ for even k and $r_{\min} = 1$ for odd k , and $\{n_m\}$ lists the enabled spatial harmonics in descending order (parity matched to k), $M(k) = \lceil \frac{k}{2} \rceil$. The calibration matrix (local Jacobian) is

$$(A_q)_{ij} = \left. \frac{\partial \Gamma_{r_i,q}}{\partial \theta_q^{(n_j)}} \right|_{\theta_q=0},$$

so that the small-phase linearization reads $\Gamma_q(\theta_q) = A_q \theta_q + \mathcal{O}(\|\theta_q\|^2)$, with A_q locally lower-triangular under the ordering above. Operationally, single-harmonic poke tests provide the diagonal entries of A_q directly, and (if desired) dominant off-diagonal terms can be measured by two-tone pokes; see below. In what follows we use A for the local Jacobian that maps second-pass phase depths to polynomial coefficients; we write A_q for clique windows and $A_{j,m}$ for KAN ridge windows; see Sec. III.

Two-bounce relay and isolation of clique sums.

The physical realization uses a single folded $4f$ relay inserted after the spin-encoding SLM, depicted in Fig. (1). The first lens L_1 Fourier-transforms the SLM-modulated field. The k SLM macropixels belonging to clique q are addressed so that their diffracted beams overlap in the same small window of the L_1 focal plane; the on-axis complex field in that window is proportional to the coherent sum of the k spin-encoded fields and, after binarization, proportional to S_q . Distinct cliques are assigned to disjoint, nonoverlapping windows. The second lens L_2 re-images the focal pattern back onto the same SLM, mapping each window to an independent phase patch that applies a clique-specific profile $\phi_q(y; \theta_q)$. Although the propagation and masking are linear in the optical field, the two-pass transfer produces an output intensity that is a nonlinear function of θ_q through the resolvent dependence of the scattering operator. This nonlinearity induces a tunable univariate mapping of S_q in each window and, by standard adjoint-Jacobian measurements, yields all parameter gradients from two optical frames per update (forward + adjoint) [45–47]. Concretely, the first-pass hologram maps spin phases $s_i \in \pm 1$ to a real on-axis field in window q proportional to $\sum_{i \in q} s_i$, with a single global calibration factor set once by flashing all +1 and all -1 patterns. Figure 1 illustrates the physical realization of the two-bounce relay.

Second-pass phase basis and parity rule. To match the parity of the target clique polynomial, we select only even (odd) spatial harmonics when k is even

(odd), ensuring that the window-averaged intensity contains only the corresponding even (odd) powers of S_q . On the second pass, the clique- q window illuminates a dedicated SLM patch with a real, y -periodic phase profile $\phi_q(y)$. Here y denotes the in-patch coordinate along the grating direction. The parity selection rule follows from the small-phase expansion of the second-pass transmittance,

$$\exp\{i\phi_q(y)\} = 1 + i\phi_q - \frac{1}{2}\phi_q^2 - \frac{i}{6}\phi_q^3 + \dots \quad (12)$$

Each power ϕ_q^p is a product of cosines that reduces (via product-to-sum) to cosines at integer combinations of the spatial frequencies $\{n_m k_0\}$. After L_2 , only the zero-spatial-frequency (DC) contribution survives the window average, so the detectable terms are precisely those products that contain a DC component. Choosing $n_m = 2m - \delta$ with $\delta \equiv k \bmod 2$ ensures that the lowest-order DC terms arise from even products when k is even and from odd products when k is odd. Consequently, the window intensity $I_q(S_q; \theta_q)$ contains only even powers of S_q for even k and only odd powers for odd k . Therefore, we write φ_q as a truncated cosine series with small depths,

$$\phi_q(y; \theta_q) = \sum_{m=1}^{M(k)} \theta_q^{(n_m)} \cos(n_m k_0 y), \quad (13)$$

where $k_0 = 2\pi/\Lambda$ is chosen commensurate with the SLM pixel grid so that an integer number Λ of pixels spans one cosine period within the patch aperture.

Odd-parity cliques and homodyne bias. With phase-only modulation on the second pass and direct intensity detection, the window-averaged response obeys the symmetry $I_q(S_q; \theta_q) = I_q(-S_q; \theta_q)$; hence only even powers of S_q appear. To represent odd-parity targets (odd k), we break this symmetry by adding a weak, coherent local-oscillator (LO) field in window q . Let the on-axis signal field after the two passes be $E_{\text{sig}}(S_q; \theta_q) \approx \alpha_q S_q + \mathcal{O}(S_q^3)$ and inject $E_{\text{LO}} = \rho e^{i\varphi}$ with $\rho \ll 1$ and phase φ aligned with α_q . On array platforms (Sec. IV) we use one weak LO per bank with a single phase setting; within a bank the linear coefficient sign is set electronically. The detected intensity becomes

$$|E_{\text{sig}} + E_{\text{LO}}|^2 = |E_{\text{sig}}|^2 + \rho^2 + 2\rho \text{Re}\{E_{\text{sig}} e^{-i\varphi}\}. \quad (14)$$

The even-order terms in $|E_{\text{sig}}|^2$ are unaffected by φ , and the ρ^2 contribution is just a constant offset. Thus tuning φ adjusts the odd-parity linear coefficient without suppressing the even-order contributions.

Local Jacobian, poke-test calibration, and constructive seeding Order the parity-matched monomials as S_q^k, S_q^{k-2}, \dots and the second-pass harmonics as $n_{M(k)}, n_{M(k)-1}, \dots$. The Jacobian from harmonic depths $\{\theta_q^{(n)}\}$ to polynomial coefficients $\{\Gamma_{r,q}\}$ is locally lower-triangular at $\theta_q = 0$: the highest spatial harmonic chiefly

controls the highest power of S_q , the next harmonic controls the next power, and so forth. Because there are exactly $M(k) = \lceil k/2 \rceil$ non-constant monomials of the same parity as k up to degree k , $M(k)$ independent phase depths per window suffice to set all non-constant coefficients.

For clique window q and harmonic n , set all second-pass phases to zero, choose a spin pattern that realizes a prescribed S_q , and record the reference intensity $I_{0,q}$. Then enable only harmonic n with a small depth change $\Delta\theta$ and measure the new intensity I_q . The difference

$$\Delta I_q(S_q) \equiv I_q - I_{0,q} \approx \kappa_n a_{nn} (\Delta\theta)^2 S_q^n, \quad (15)$$

yields the diagonal gain $a_{nn} > 0$ directly:

$$a_{nn} = \frac{\Delta I_q(S_q)}{\kappa_n (\Delta\theta)^2 S_q^n}. \quad (16)$$

Here κ_n is a calibration constant set by the relay geometry and windowing. If a weak homodyne LO is present, odd powers in S_q can be selected and linear-in-depth terms appear in the mixed signal; in the default calibration we keep the LO off and use the quadratic-in-depth response. Repeating the poke over all n and windows gives the diagonal of the locally lower-triangular map

$$\Gamma_q = A_q \theta_q + \mathcal{O}(|\theta_q|^2). \quad (17)$$

If desired, dominant off-diagonals of A_q can be estimated by exciting two harmonics simultaneously and subtracting the two single-poke responses; for the refinement step, the diagonal calibration is typically sufficient.

Form the target coefficient vector $c_q = (c_{k,q}, c_{k-2,q}, \dots)^\top$, from the clique polynomial Φ_q . Solve the triangular system $A_q \theta_q \approx \alpha_q c_q$ by forward substitution from degree k down to r_{\min} . The overall scale α_q is absorbed into the per-clique gain w_q . A short refinement using two-frame adjoint gradients (two optical frames per update, all parameters simultaneously) then compensates higher-order mixing and measurement noise.

Worked example: $k = 4$ (even parity), small-phase mixing, and closed-form seeding. For a 4-spin clique q , the product reduces to an even univariate polynomial of the clique sum $S_q = \sum_{i \in q} s_i$: $\prod_{i \in q} s_i = \Phi_q(S_q) = \frac{1}{24} S_q^4 - \frac{2}{3} S_q^2 + 1$. With a 4-local coupling J_q , the target contribution is $J_q \Phi_q(S_q)$. Dropping the constant term, the coefficients to realize are

$$a_q = \frac{J_q}{24} \text{ for } S_q^4, \quad b_q = -\frac{2}{3} J_q \text{ for } S_q^2. \quad (18)$$

Use the parity-matched two-harmonic patch

$$\begin{aligned} \phi_q(y) &= \theta_q^{(2)} \cos(2k_0 y) + \theta_q^{(4)} \cos(4k_0 y), \\ \alpha &\equiv \theta_q^{(2)}, \quad \beta \equiv \theta_q^{(4)}, \end{aligned} \quad (19)$$

which multiplies the carrier pair $E_{\text{in}}(y) \propto S_q(e^{ik_0 y} + e^{-ik_0 y})$ on the second pass. We will work in the small-phase regime $|\alpha|, |\beta| \ll 1$.

Expanding $e^{i\phi_q(y)}$ with $e^{ia \cos \theta} = \sum_m i^m J_m(a) e^{im\theta}$ and using $J_1(x) \approx x/2$, $J_2(x) \approx x^2/8$ for small arguments, the leading returns to the $\pm k_0$ bank are as follows. At the order α^2 , there are two symmetric paths via $\pm 2k_0$, contributing $2J_1(\alpha)^2 = \frac{1}{2}\alpha^2$. At the order β^2 , there are three quadratic channels via $\pm 4k_0$, contributing $3J_1(\beta)^2 = \frac{3}{2}\beta^2$. At the mixed (cubic) term there are two $\pm 2k_0$ hops plus one $\mp 4k_0$ hop, giving $2J_2(\alpha)J_1(\beta) = \frac{1}{8}\alpha^2\beta$. Window averaging promotes these returns to even powers of S_q in the intensity. Grouping geometry/detection factors into calibration gains yields the linear relations below.

Let $a_{22}, a_{42}, a_{44} > 0$ be the calibrated gains that convert the listed depth combinations into the S_q^2 and S_q^4 coefficients of the window-averaged intensity. Then

$$\begin{aligned} (\text{for } S_q^2) \quad & a_{22} \frac{1}{2} \alpha^2 + a_{42} \frac{3}{2} \beta^2 = b_q, \\ (\text{for } S_q^4) \quad & a_{44} \frac{1}{8} \alpha^2 \beta = -a_q. \end{aligned} \quad (20)$$

The first line gathers the α^2 and β^2 returns to $\pm k_0$ that map into the quadratic coefficient; the second isolates the leading mixed contribution to the quartic coefficient. Eliminate $\beta = -\frac{8a_q}{a_{44}\alpha^2}$ and set $y = \alpha^2$ to obtain the cubic

$$a_{22}y^3 - 2b_qy^2 + \frac{192a_{42}a_q^2}{a_{44}^2} = 0. \quad (21)$$

Divide by a_{22} and substitute $y = z + \frac{2b_q}{3a_{22}}$. With

$$\begin{aligned} P &= -\frac{1}{3} \left(\frac{2b_q}{a_{22}} \right)^2, \quad Q = \frac{192a_{42}a_q^2}{a_{22}a_{44}^2} - \frac{2}{27} \left(\frac{2b_q}{a_{22}} \right)^3, \\ \Delta &= \left(\frac{Q}{2} \right)^2 + \left(\frac{P}{3} \right)^3, \end{aligned} \quad (22)$$

Cardano's formula gives

$$\begin{aligned} z &= \sqrt[3]{-\frac{Q}{2} + \sqrt{\Delta}} + \sqrt[3]{-\frac{Q}{2} - \sqrt{\Delta}}, \quad \alpha = \sqrt{z + \frac{2b_q}{3a_{22}}}, \\ \beta &= -\frac{8a_q}{a_{44}\alpha^2}. \end{aligned} \quad (23)$$

We take the principal complex square-root in $\sqrt{\Delta}$ and the real cubic roots in Cardano's expression so that $\alpha, \beta \in \mathbb{R}$; this choice matches the small-phase regime used during calibration. This closed-form seed is typically accurate to the percent level. A short refinement with physically measured gradients then compensates residual cross-couplings. This forward substitution yields a better seed than the diagonal-only version. It is still a first-order, small-phase approximation. In practice we either drop off-diagonal terms and use the diagonal-calibrated seed, or measure leading off-diagonal terms

(e.g., via a two-harmonic poke) and solve the triangular pair for a tighter seed; both paths converge quickly after refinement as Fig. 2 illustrates.

Learning rule and physical gradients. For each clique q , define the centred target $\tilde{I}_q(S) = \Phi_q(S) - \Phi_q(0)$, where $S \in \mathcal{S}_k = \{-k, -k+2, \dots, k\}$ denotes a dummy variable ranging over the admissible values of $S_q = \sum_{i \in q} s_i$. Fit the per-window response by minimizing

$$\mathcal{L}(\{\theta_q, w_q\}) = \frac{1}{2} \sum_{q \in \mathcal{C}_k} \sum_{S \in \mathcal{S}_k} [w_q I_q(S; \theta_q) - \tilde{I}_q(S)]^2. \quad (24)$$

Here $\theta_q = \{\theta_q^{(n)}\}_{n \in \{n_m\}}$ collects the second-pass phase depths for the parity-matched harmonics $n_m = 2m - \delta$ in window q , and w_q is a scalar gain. Physical gradients $\partial I_q / \partial \theta_q^{(n)}$ are obtained from two auxiliary camera frames via the adjoint–Jacobian protocol for the scattering operator. With these gradients, steepest-descent updates of $\{\theta_q\}$ and $\{w_q\}$ converge rapidly. Because Fourier-plane windows are optically isolated, the optimization decouples across cliques aside from shared hyperparameters (learning rates and stopping criteria).

The loss \mathcal{L} is quadratic and, therefore, convex in the linear weights $\{w_q\}$ for fixed optical parameters $\{\theta_q\}$. As a function of $\{\theta_q\}$, convexity is regime-dependent. In the small-phase regime the window-averaged response $I_q(S; \theta_q)$ is well approximated by a parity-matched truncated even polynomial in the control amplitudes, so the residuals are effectively linear in $|\theta_q|^2$; under this approximation \mathcal{L} remains convex and gradient descent reaches the global minimizer. Beyond the perturbative regime, higher-order Bessel contributions render I_q nonlinear in θ_q , so the joint problem is only locally convex. In practice, (i) poke-test calibration of the local Jacobian, (ii) restricting $|\theta_m| \lesssim 1$, and (iii) initialization from the closed-form seeds keep the iterates inside the convex basin; each clique then behaves like a well-conditioned convex regression, and convergence to the desired coefficients is fast and reliable.

Numerical simulations aligned with calibration.

We simulate the calibration–refinement workflow and depict the result in Fig. 2. For each $k \in \{3, \dots, 15\}$ we form the target coefficient vector $c_k = (c_k, c_{k-2}, \dots)^\top$, where $\{c_r\}$ are the parity-restricted coefficients of the unique degree- $\leq k$ polynomial that interpolates the k -spin product on $\mathcal{S}_k = \{-k, -k+2, \dots, k\}$ (the constant is dropped).

Near the small-phase operating point the device is described by a lower-triangular map from harmonic depths to polynomial coefficients,

$$\Gamma(\theta) = A\theta + \mathcal{O}(|\theta|^2), \quad \Gamma = (\Gamma_k, \Gamma_{k-2}, \dots)^\top, \quad (25)$$

with $M(k) = \lceil k/2 \rceil$ coefficients and the same number of trainables. In this subsection we analyze a single representative window, and for notational brevity we sup-

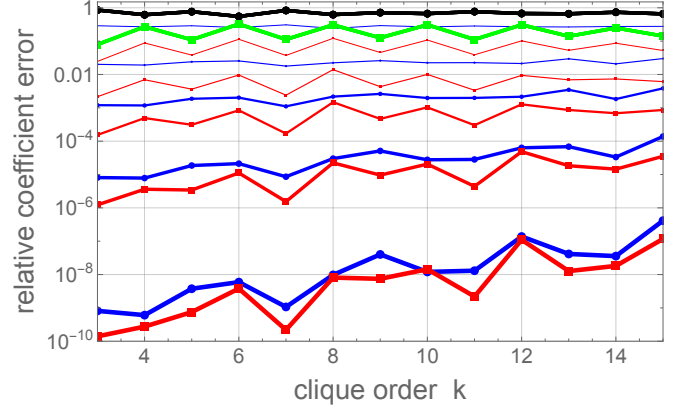


FIG. 2. Mean relative coefficient error versus clique order k , averaged over 10 realizations. For each $k \in \{3, \dots, 15\}$ we form the parity-matched target vector $c_k = (c_k, c_{k-2}, \dots)^\top$ by interpolating the k -spin product on $\mathcal{S}_k = \{-k, -k+2, \dots, k\}$ (constant term excluded). The device map is drawn as a random lower-triangular A with positive diagonal, entries $a_{ii} \sim \text{Unif}[1.6, 2.4]$ and $a_{ij} \sim \text{Unif}[0.6, 1.4]$ for $i > j$, and realizations with condition number $\kappa(A) > 5$ are rejected. We report the relative coefficient error $\varepsilon_{\text{rel}} = \|A\theta - c_k\|_2 / \|c_k\|_2$ using the noiseless linearized map $\Gamma = A\theta$. Each trace shows the mean over 10 realizations for $n_{\text{iter}} \in \{10, 50, 100, 200, 400\}$ steepest-descent steps ($\eta = 0.03$) from either the naive seed $\theta = c_k$ (black) or the diagonal-calibrated seed $\theta = c_k / \text{diag}(A)$ (green); blue and red traces show the same seeds (blue for the naive seed and red for the diagonal-calibrated seed) followed by gradient refinement. The thickness of the blue and red lines is proportional to n_{iter} . Diagonal calibration reduces the initial error by about one decade, and refinement drives it to 10^{-3} – 10^{-4} once $n_{\text{iter}} \gtrsim 100$, with weak dependence on k owing to the bounded conditioning of A .

pressed the window index q ; here A is precisely the per-window Jacobian A_q . For Fig. 2 we draw $A \in \mathbb{R}^{M \times M}$ as a random lower-triangular matrix with positive diagonal: each entry is sampled uniformly from $[0.6, 1.4]$ and then the diagonal is incremented by 1. Thus $a_{ii} \sim \text{Unif}[1.6, 2.4]$ and $a_{ij} \sim \text{Unif}[0.6, 1.4]$ for $i > j$. This construction yields a well-conditioned triangular system with modest sub-diagonal mixing. Realisations with the condition number $\kappa(A) > 5$ are rejected and redrawn. For each k we average over 10 independent draws.

We optimize the coefficient-space loss

$$\mathcal{L}(\theta, w) = \frac{1}{2} \|w A\theta - c_k\|_2^2, \quad (26)$$

and report the relative coefficient error

$$\varepsilon_{\text{rel}} = \frac{\|A\theta - c_k\|_2}{\|c_k\|_2}. \quad (27)$$

Starting with either (i) naive seed $\theta = c_k$ or (ii) diagonal-calibrated seed $\theta = c_k / \text{diag}(A)$ (elementwise division) we implement for $n_{\text{iter}} \in \{10, 50, 100, 200, 400\}$

the steepest-descent steps with step size $\eta = 0.03$ on $\mathcal{L}(\theta, 1)$.

To isolate the algorithmic behavior in Fig. (2), the plotted runs use the noiseless linear map $\Gamma = A\theta$. Diagonal calibration alone lowers the mean initial error by about one decade relative to the naive seed for all k (the black and green traces start at $\mathcal{O}(1)$). Adding refinement drives the mean error into the 10^{-3} – 10^{-4} range once $n_{\text{iter}} \gtrsim 100$, with little dependence on k because the parameter count and spectrum scale only with $M(k) = \lceil k/2 \rceil$ and we cap $\kappa(A)$ at 5. When quadratic terms in Γ become non-negligible, halving $|\theta|$, re-linearizing A around the current point, and continuing restores linear-rate progress and the same error bands.

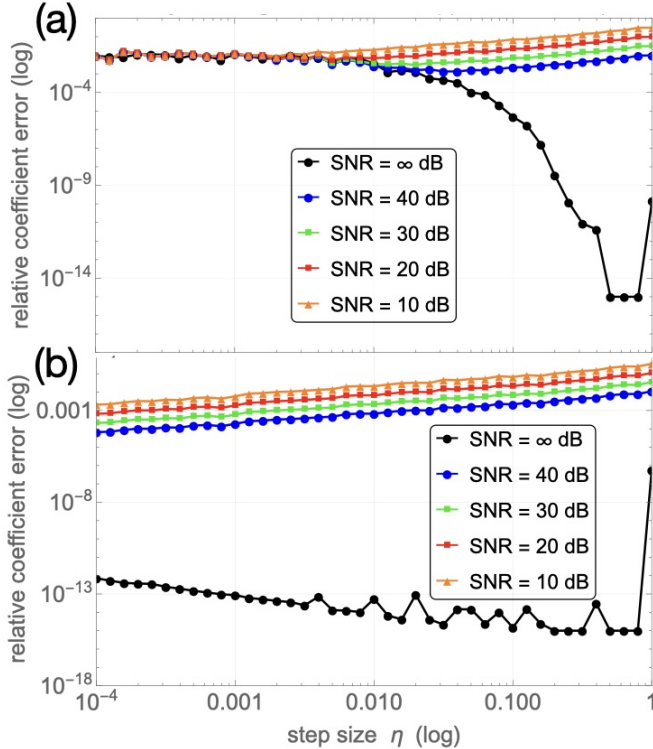


FIG. 3. **Step-size dependence at fixed clique order $k = 10$ under noisy simulations.** For a $k = 10$ clique we form the parity-matched target coefficient vector c (non-constant terms only) and use the diagonal-calibrated seed followed by the gradient descent solver: seed $\theta_0 = c/\text{diag}(A)$ and iterate $\theta \leftarrow \theta - \eta A^\top r^{\text{meas}}$ with residual $r^{\text{meas}} = (A\theta - c) + \xi$. The device map A is drawn once per seed as a lower-triangular, well-conditioned matrix with positive diagonal and fabrication jitter: entries are multiplied by $1 + \delta$ with $\delta \sim \mathcal{N}(0, \sigma_A^2)$ ($\sigma_A = 0.05$). Measurement noise ξ is i.i.d. Gaussian with per-component standard deviation set by an σ_ξ given by Eq. (28). We plot the relative coefficient error ε_{rel} given by Eq. (27). Each curve shows the mean over 10 seeds; markers indicate the sampled values of η . (a) Fixed iteration budget $n_{\text{iter}} = 100$. (b) Equalized optimization horizon $n_{\text{iter}}(\eta) = \lceil 50/\eta \rceil$.

Next we establish the effect of the noise. For a fixed

clique order k , we evaluate diagonal-calibrated seed followed by the gradient decent refinement using a lower-triangular device map A with positive diagonal and multiplicative fabrication jitter (drawn once per seed), and with per-iteration measurement noise in the residual, $r^{\text{meas}} = (A\theta - c) + \xi$. The noise level is parameterized by signal-to-noise ratio (SNR) (in dB) via

$$\sigma_\xi = \|c\|_2 / \sqrt{\dim(c) 10^{\text{SNR}/10}}. \quad (28)$$

Performance is reported as the relative coefficient error Eq. (27). We compare two protocols at a fixed clique size $k = 10$: (i) a fixed iteration budget $n_{\text{iter}} = 100$ and (ii) an equalized horizon $n_{\text{iter}}(\eta) = \lceil 50/\eta \rceil$ that keeps the effective continuous-time window constant. See Fig. 3(a–b).

With a fixed iteration budget [Fig. 3(a)], larger η reduces the clean (∞ dB) error by accelerating contraction per step, but with finite SNR the same η amplifies noise at each update so the final error rises: a “U-turn” trend that worsens at lower SNR. With an equalized horizon $n_{\text{iter}}(\eta) = \lceil 50/\eta \rceil$ [Fig. 3(b)], the clean curve still gradually decays, while noisy curves appear as straight lines on the log-log axes with nearly constant slope: steady-state error scales as $\|A\theta - c\| \propto \sqrt{\eta}$ (variance $\propto \eta$), producing parallel power-law lines offset by SNR. Even without measurement noise, the ∞ dB curve eventually exhibits a U-turn at large $\eta = \mathcal{O}(1)$: gradient descent on a quadratic is stable only for $\eta < 2/\lambda_{\text{max}}(A^\top A)$. As η approaches this bound, the contraction factor worsens and overshooting causes oscillations, so the final error increases again. Thus, both clean and noisy runs display an optimal intermediate η : in the clean case it is set by the stability limit of A , while in noisy cases it is set by the trade-off between faster contraction and stronger noise amplification. Overall, the lowest noisy error is obtained with the smallest stable η and longer runs; large η is advantageous only in the clean limit or when iteration budgets are tightly capped.

III. ALL-OPTICAL IMPLEMENTATION OF KOLMOGOROV-ARNOLD NETWORKS

Section II showed that one folded two-bounce relay yields independently programmable univariate polynomials per spatial window. The same primitive implements Kolmogorov-Arnold networks (KANs), which realize each output as a finite sum of learnable univariate ridge functions acting on linear projections:

$$F_j(x) = \sum_{m \in \mathcal{M}_j} \Phi_{j,m}(w_{j,m}^\top x), \quad j = 1, \dots, K, \quad (29)$$

with learnable projections $w_{j,m} \in \mathbb{R}^d$ and univariate maps $\Phi_{j,m} : \mathbb{R} \rightarrow \mathbb{R}$. Here \mathcal{M}_j indexes the ridges in

output bank j and $M_j = |\mathcal{M}_j|$. Throughout Secs. II–III we index spatial harmonics on the second pass by $n \in R_{j,m}$, and polynomial degrees in the scalar argument $z_{j,m} = w_{j,m}^\top x$ by $r \in P_{j,m}$. We denote $R_{j,m} \equiv |R_{j,m}|$ and $P_{j,m} \equiv |P_{j,m}|$. The small-depth linearization of the per-window map is

$$\Gamma_{r,jm}(\theta_{j,m}) = \sum_{n \in R_{j,m}} A_{j,m}[r, n] \theta_n(j, m) + \mathcal{O}(|\theta_{j,m}|^2), \quad (30)$$

so that $A_{j,m} \in \mathbb{R}^{P_{j,m} \times R_{j,m}}$ is the local Jacobian (evaluated at $\theta_{j,m} = 0$) from harmonic depths to polynomial coefficients. We reserve n exclusively for harmonics and r exclusively for polynomial orders.

When piecewise segmentation is used, a ridge window may be partitioned into $G \geq 1$ sub-windows whose outputs are optically summed. This factorization mirrors the optics of Sec. II: diffraction computes many projections in parallel; a per-window structural nonlinearity implements the univariate maps independently and simultaneously. The free-space realization of (29) is sketched in Fig. 4. When each ridge uses a single global polynomial (no segmentation), the $G=1$ variant is shown in Fig. 5.

Free-space SPIM realisation of a one-layer KAN. *First pass (projections).* The first SLM pass displays a hologram T_1 that directs the on-axis field in Fourier-plane window (j, m) to a real amplitude proportional to $z_{j,m} = w_{j,m}^\top x$, with disjoint windows separated by guard bands as in Sec. II. See the fan-out into disjoint Fourier-plane windows and their grouping into banks in Fig. 4.

Second pass (per-ridge nonlinearity). A folded 4f relay re-images the Fourier plane onto dedicated second-pass patches on the same SLM, one patch per window. The (j, m) patch carries a small-depth, parity-matched cosine basis

$$\phi_{j,m}(y) = \sum_{n \in R_{j,m}} \theta_n^{(j,m)} \cos(nk_0 y), \quad |\theta_n^{(j,m)}| \ll 1. \quad (31)$$

Window averaging and the small-phase expansion yield a polynomial response in the projection amplitude

$$I_{j,m}(\theta_{j,m}; z_{j,m}) = \Gamma_{0,jm}(\theta_{j,m}) + \sum_{r=1}^{R_{j,m}} \Gamma_{r,jm}(\theta_{j,m}) z_{j,m}^r. \quad (32)$$

With direct intensity readout, only even powers appear by default; odd powers are enabled, when needed, by adding a weak local-oscillator in that window exactly as in Sec. II. The parity of $R_{j,m}$ is selected to match the desired parity of $\Phi_{j,m}$. The per-window second-pass patches that realize the ridge nonlinearities are indicated in Fig. 4; the special case with one segment per ridge ($G=1$) corresponds to Fig. 5.

Readout (banked sums). The output of layer j is formed by summing the ridge channels assigned to that

output after subtracting constant offsets:

$$y_j = \sum_{m \in \mathcal{M}_j} [I_{j,m}(\theta_{j,m}; z_{j,m}) - \Gamma_{0,jm}], \quad (33)$$

realizing (29) with $\Phi_{j,m}$ represented by the calibrated map $z \mapsto I_{j,m}(\theta_{j,m}; z)$ on its operating interval. The banked optical summation (constants subtracted) is shown schematically in Fig. 4.

Calibration and learning (per window). Calibration reuses Sec. II. For each window (j, m) , single-harmonic poke tests measure the locally lower-triangular map with the elements

$$A_{j,m}[r, n] = \left. \frac{\partial(\Gamma_{r,jm})}{\partial(\theta_n^{(j,m)})} \right|_{\theta=0}, \quad (34)$$

ordered so that higher spatial harmonics primarily set higher powers of $z_{j,m}$. Forward substitution then provides an analytic seed for $\theta_{j,m}$ that matches the target ridge coefficients up to an overall scale (absorbed into a per-ridge gain). Refinement uses two-frame adjoint gradients to obtain $\partial I_{j,m} / \partial \theta_r^{(j,m)}$ for all parameters simultaneously. In the software experiments of this section we emulate the hardware measurement by a finite-difference (FD) proxy for clarity; see Eq. (41).

Alternative structural-nonlinearity realization (nPOLO). Instead of a second pass, the same SLM can be traversed N times with a folding mirror and per-bounce, piecewise-affine masks $T_n(y) = \exp\{i(s_n y + b_n)\}$. The detected intensity after N bounces is a polynomial in z whose coefficients are explicit functions of $\{s_n, b_n\}_{n=1}^N$. Partitioning the SLM into sub-apertures yields independent ridge channels; increasing N increases the achievable polynomial degree. The trade-off relative to the two-pass relay is locality: in the multi-bounce design the parameters of a given bounce are shared across all illuminated pixels unless the aperture is partitioned, whereas in the two-pass relay the coefficient control is per-window local by construction. The layer topology remains that of Fig. 4; only the block implementing the per-window map $z \mapsto I_{j,m}(\theta_{j,m}; z)$ changes from a two-pass relay to an N -bounce (nPOLO) stack.

Numerical test (teacher–student). We illustrate the method in a controlled teacher–student experiment: a single KAN layer with per-window structural nonlinearity and a calibrated small-phase model learns its teacher efficiently using either exact model gradients or two-frame finite-difference (physical) gradients. Figure 6 illustrates our findings. All simulations use the $G=1$ configuration of Fig. 5; odd powers (when required) are enabled by the weak LO as in Sec. II.

Teacher. The teacher is a one-layer ridge expansion with $d = 8$ inputs and $M = 8$ ridges,

$$y(x) = \sum_{m=1}^8 \Phi_m(w_m^\top x), \quad x \in [-1, 1]^8, \quad (35)$$

where $W = [w_1, \dots, w_8]$ has orthonormal columns. Ridge parities alternate even/odd. Even ridges use $\Phi_m(z) = c_{4,m}z^4 + c_{2,m}z^2$; odd ridges use $\Phi_m(z) = c_{3,m}z^3 + c_{1,m}z$. Coefficients are chosen so outputs remain well scaled on $z \in [-1, 1]$.

Student model. The student shares the same projections and parity but learns per-window polynomial coefficients through a calibrated, locally lower-triangular map from control variables to effective polynomial weights. For ridge m , let $z_m = w_m^\top x$ and use exponents $\{r_1, r_2\} = \{4, 2\}$ (even) or $\{3, 1\}$ (odd). The ridge output is

$$I_m(\theta_m; z_m) = \Gamma_{0,m} + \Gamma_{r_1,m}(\theta_m)z_m^{r_1} + \Gamma_{r_2,m}(\theta_m)z_m^{r_2}, \quad (36)$$

with calibrated linearization

$$\Gamma_m(\theta_m) = A_m \theta_m, \quad A_m \in \mathbb{R}^{2 \times 2}, \quad (37)$$

whose diagonal entries are ≈ 1 and off-diagonals are small (one draw per ridge with $\kappa(A_m) \leq 5$). At readout we subtract the constant offsets, so

$$\hat{y}(x) = \sum_{m=1}^8 \left[I_m(\theta_m; z_m) - \Gamma_{0,m} \right] = \sum_{m=1}^8 \sum_{i=1}^2 \Gamma_{r_i,m}(\theta_m) z_m^{r_i}, \quad (38)$$

exactly as in Eq. (33).

Data, loss, and initialization. We use $B = 4096$ i.i.d. inputs $x^{(b)} \sim \text{Unif}([-1, 1]^8)$ with targets $y^{(b)} = y(x^{(b)})$, plus a disjoint test set of the same size. The loss is

$$\mathcal{L} = \frac{1}{B} \sum_{b=1}^B (\hat{y}(x^{(b)}) - y(x^{(b)}))^2. \quad (39)$$

We seed from the diagonal calibration,

$$\theta_m^{(0)} = \text{diag}(A_m)^{-1} \begin{bmatrix} c_{\text{high},m} \\ c_{\text{low},m} \end{bmatrix}, \quad (40)$$

with $c_{\text{high},m} \equiv c_{4,m}$, $c_{\text{low},m} \equiv c_{2,m}$ (even) and $c_{\text{high},m} \equiv c_{3,m}$, $c_{\text{low},m} \equiv c_{1,m}$ (odd).

Optimization modes. Fixed-step steepest descent is run in two modes: (i) exact gradients of the calibrated linear model; (ii) ‘two-frame’ physical gradients as realized in hardware by the adjoint protocol (two optical frames per update for all parameters). In this software-only demonstration we emulate the hardware measurement by a FD proxy: central differences applied to each parameter

$$\frac{\partial \mathcal{L}}{\partial \theta_{m,j}} \approx \frac{\mathcal{L}(\theta_{m,j} + \delta) - \mathcal{L}(\theta_{m,j} - \delta)}{2\delta}, \quad \delta = 10^{-4}, \quad (41)$$

with step sizes $\eta = 0.05$ (i) and $\eta = 0.1$ (ii). The software cost is two evaluations per parameter, whereas the hardware cost remains two frames per update.

Teacher coefficients.

m	degrees	$[c_{\text{high}}, c_{\text{low}}]$
1	[4, 2]	[-0.060, 0.401]
2	[3, 1]	[-0.239, 0.516]
3	[4, 2]	[0.283, -0.382]
4	[3, 1]	[0.263, -0.558]
5	[4, 2]	[-0.057, -0.724]
6	[3, 1]	[0.041, -0.659]
7	[4, 2]	[0.040, -0.269]
8	[3, 1]	[0.282, -0.676]

Results. Figure 6 visualizes the outcomes. In panel 6(a) (semilog MSE vs. iteration), the four traces start at $\text{MSE} \approx 2.89 \times 10^{-4}$ and by $t = 400$ end at 1.64×10^{-7} (train, exact) and 1.89×10^{-7} (test, exact), and at 6.89×10^{-9} (train, two-frame) and 8.92×10^{-9} (test, two-frame), showing similar convergence rates with a lower asymptotic floor for two-frame updates. Panel 6(b) reports the per-ridge relative coefficient error $\varepsilon_m = \|A_m \theta_m - c_m\|_2 / \|c_m\|_2$: the initialization spans 3.2×10^{-5} – 3.298×10^{-2} , while after exact-gradient training the errors fall to 5.8×10^{-5} – 2.96×10^{-3} . Panels 6(c)–(d) overlay the learned ridge responses $I_m(z)$ (orange) on the teacher $\Phi_m(z)$ (blue) for a representative even ridge ($m = 1$) and odd ridge ($m = 2$), showing visual indistinguishability on $z \in [-1, 1]$ and correct parity. The normalized test RMSE over the held-out set is $\text{nRMSE} \approx 6.39 \times 10^{-4}$ (exact) and $\approx 1.39 \times 10^{-4}$ (two-frame), consistent with panel 6(a). Finally, the note on N_{enc} (number of mask encounters/bounces) is orthogonal to Fig. 6: increasing N_{enc} raises the maximum usable polynomial degree before the small-phase model saturates.

IV. PROGRAMMABILITY ON VCSEL ARRAYS AND ON THE AOC

Having established in Secs. II–III that a folded 4f relay plus per-window second-pass patches implements independently programmable univariate responses (for both clique polynomials and KAN ridges), we now show that the same primitive ports verbatim to injection-locked VCSEL arrays and to the analog optical computer (AOC). The hardware insert is identical, and the calibration/learning loop carries over unchanged. The windowing and banked-sum layout follow Fig. 4.

VCSEL arrays under injection lock. Injection locking provides a mutually coherent multi-emitter source, so the first pass computes the banked projections $z_{j,m}$ in disjoint Fourier-plane windows exactly as on SPIM. The same folded 4f relay assigns a dedicated second-pass patch to each window and realizes the per-window nonlinearity $I_{j,m} \approx \Phi_{j,m}(z_{j,m})$ as in Eq. (32). Ridge outputs belonging to the same bank j are then optically summed to form y_j after subtracting constants,

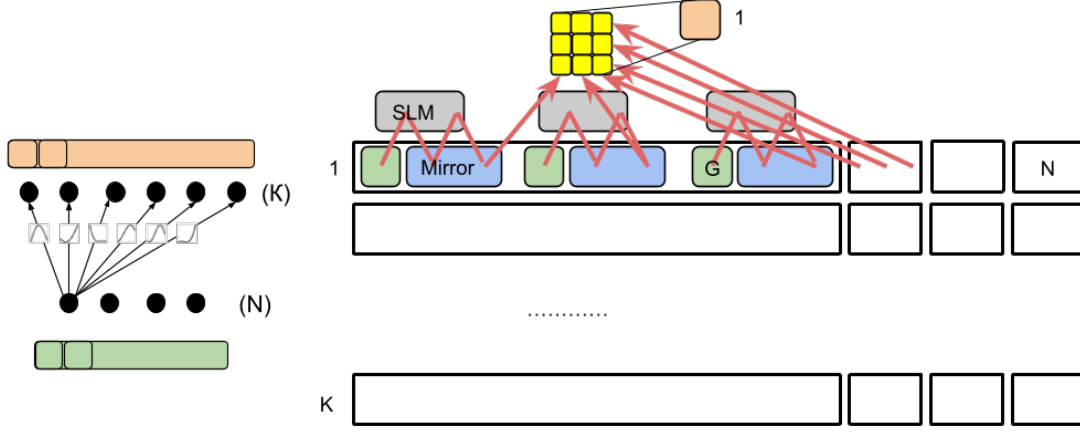


FIG. 4. **Schematic of a shallow $[N, K]$ all-optical KAN layer.** Inputs $x \in \mathbb{R}^N$ are encoded on the first SLM; a holographic fan-out computes the projections $z_{j,m} = w_{j,m}^\top x$ and directs them to disjoint Fourier-plane windows grouped into K banks (one bank per output y_j), cf. Eq. (29). Each ridge window may be partitioned into $G \geq 1$ sub-windows to implement a piecewise-polynomial (or spline) approximation to $\Phi_{j,m}(\cdot)$. The local nonlinearity in each sub-window is realized optically, either by the two-pass folded $4f$ relay of Section II or by a multi-bounce (nPOLO) block, yielding a calibrated per-window map $z \mapsto I_{j,m}(\theta_{j,m}; z)$ as in Eqs. (31)–(33). With direct intensity readout, even powers appear by default; a weak bank-wise LO enables odd orders. Sub-windows belonging to the same ridge are re-imaged and optically summed; the output y_j is obtained by summing ridge channels in bank j after subtracting constants (Eq.(33)). With $M_j = N$ ridges per output, the configuration instantiates $G \times N \times K$ optical channels.

following the readout in (33). Per-channel gains are set once by flashing each window in turn.

Calibration and learning are identical to SPIM. Single-harmonic poke tests measure the locally lower-triangular map $A_{j,m}$ from second-pass depths to polynomial coefficients; forward substitution provides closed-form seeds for the control depths; and in-situ refinement uses two auxiliary frames per parameter to obtain physical gradients $\partial I_{j,m} / \partial \theta_{j,m}^{(n)}$. The same primitive also programs clique-symmetric k -local Ising energies by arranging the window layout as in Sec. II and fitting the parity-restricted polynomial $\Phi_q(S_q)$ for each clique window. Odd-order ridge terms, when required, are enabled by adding a weak, bank-wise local oscillator (one shared LO phase per output bank suffices to set the linear coefficient’s sign and scale while preserving higher odd orders), as discussed in Sec. II.

Analog optical computer (AOC). On the AOC, we insert the same folded $4f$ relay between the projection SLM (that implements the OVMM) and the detector plane, partition the Fourier plane into disjoint windows, and program one second-pass patch per window as in (31). The relay realizes $\Phi(z)$ optically via (32), enabling the same in-situ, two-frame gradient measurement used on SPIM. For k -local programming the AOC uses the clique layout and parity-matched patches of Sec. II with identical calibration and learning. If odd powers are needed, a weak bank-wise LO can be introduced exactly as above.

The upshot is a unified recipe: diffraction supplies the linear projections; a per-window structural nonlinearity, either the two-pass relay or a multi-bounce nPOLO block, implements independently programmable univariate maps. The same calibrated primitive therefore programs both clique-symmetric k -local Ising energies and KAN ridge functions, carrying over unchanged from free-space SPIMs to VCSEL arrays and to the AOC.

We envision two immediate applications. *First, a single-layer all-optical KAN.* The OVMM forms $z = Wx$; the relay implements per-window ridge maps $\Phi_m(z)$ via Eqs. (31)–(33); and banked optical summation yields y . Calibration and two-frame gradient refinement follow Secs. II–III. *Second, an all-optical proximal step.* In the iteration (4), substitute per-channel optical maps $\Phi_j(s_j)$ for $f(s_j)$ so that $W\Phi(s_t)$ is produced entirely in optics, with only the scalar schedule $\alpha(t)$ and momentum γ in Eq. (4) set electronically. Both use the same per-window primitive and the same training protocol.

V. CONCLUSION AND OUTLOOK

We have presented a hardware-minimal, SLM-centric route that upgrades existing optical Ising machines to support native k -local interactions and, with the same optics, supplies the independent univariate nonlinearities required by Kolmogorov–Arnold networks. The central observation is that every k -body Ising term is a

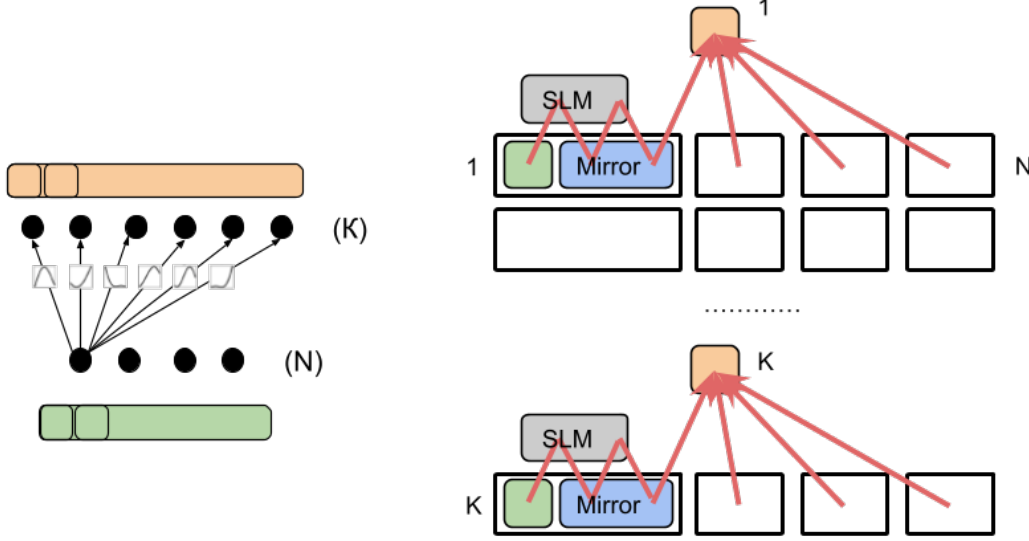


FIG. 5. **Shallow $[N, K]$ all-optical KAN with a single segment per ridge.** Each ridge window implements one global polynomial $\Phi_{j,m}$ over the full argument range ($G = 1$), reducing the channel count to $N \times K$. To maintain approximation accuracy without segmentation, either increase the number N_{enc} of mask encounters in the multi-bounce (nPOLO) block or enlarge the parity-matched harmonic set in the two-pass relay, thereby raising the effective polynomial degree in Eq. (32). When using intensity detection, a weak local oscillator can be introduced to enable odd-order terms. All other optical elements and the readout path follow Fig. 4.

parity-restricted polynomial of the clique sum, which can be realized optically as a per-window structural nonlinearity using a single folded $4f$ relay and a second programmable pass over the same SLM. The consequence is twofold. First, spatial-photonic Ising machines, injection-locked VCSEL arrays, and AOC-style architectures can embed clique-specific k -local couplings without $\chi^{(2)}$ or Kerr media. Second, the very same per-window mechanism yields hundreds of independently trainable ridge functions, enabling fully optical KAN layers with diffraction-based projections and *in-situ* learning via measured physical gradients.

On the modeling side, we formalized the reduction of a k -body product to a univariate polynomial in S_q and identified a minimal, parity-matched harmonic basis for the second SLM pass that requires only $M(k) = \lceil k/2 \rceil$ trainable phase depths per clique. The Jacobian from phase depths to polynomial coefficients is locally lower-triangular and thus invertible; closed-form seeds followed by two-frame physical-gradient descent achieve coefficient errors in the 10^{-2} – 10^{-4} range within 10^2 – 3×10^2 iterations for $3 \leq k \leq 15$, with negligible dependence on k . The same mathematical structure underpins the optical KAN: holographic fan-out supplies linear projections, and each ridge function is implemented as a calibrated per-window polynomial using the identical measurement-based gradient procedure. We also delineated a complementary multi-bounce realiza-

tion (nPOLO), where higher polynomial orders follow from increasing the bounce count; both routes are compatible with the proposed windowed, per-ridge control.

Implementation pathways were given for two platforms beyond free-space SPIMs. In VCSEL arrays, the clique engine is inserted as a parallel feedback branch that forms windowed sums under injection lock and feeds back the force proportional to $-\Phi'_q(S_q)$ uniformly to all spins in a clique via polarization-selective injection. Odd-order ridge terms are enabled bank-wise by a weak local oscillator with a single phase setting per bank. In the AOC, we insert the same folded $4f$ relay between the optical multiply and the detector plane to realize $\Phi(z)$ directly. In both cases, k -local programming and KAN ridges share the same per-window calibration and learning loop.

The present study suggests several directions for future work. Integration with recently demonstrated monolithic optical Ising machines [35] could enable chip-scale k -local processors, while incorporation of photonic KAN architectures [30] may enable hybrid optimization-learning systems. The structural nonlinearity approach aligns with recent large-scale demonstrations [39], suggesting feasibility for scaling to millions of variables. Scaling to thousands of cliques and ridges should benefit from metasurface SLMs with finer pixels and lower inter-window crosstalk, as well as from on-chip $4f$ loops that reduce loss and footprint. Distributing and stabilizing homodyne biases for odd-parity terms at scale is

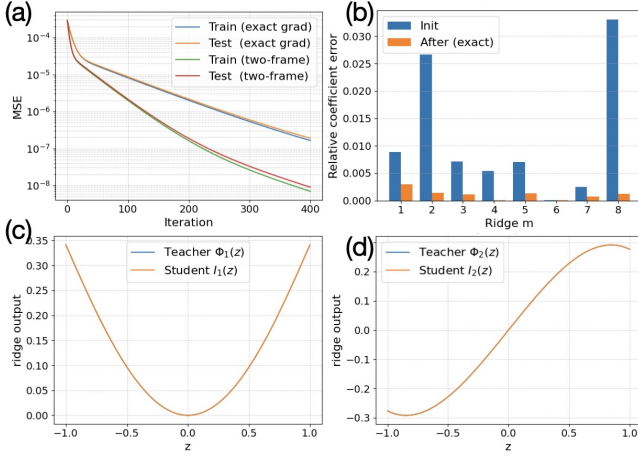


FIG. 6. **Teacher-student learning with a single KAN layer.** (a) Train/test MSE (semilog scale) for exact calibrated gradients (400 steps, step size 0.05) and two-frame gradients (400 steps, step size 0.1); ‘two-frame’ denotes the hardware adjoint protocol (two optical frames per update, all parameters simultaneously). Here we emulate it with a finite-difference proxy (FD proxy)—central differences per parameter—purely for software validation. Both modes converge within a few hundred iterations; two-frame gradients reach a lower asymptotic MSE. (b) Per-ridge relative coefficient error $\varepsilon_m = \|A_m \theta_m - c_m\|_2 / \|c_m\|_2$ at initialization and after exact-gradient training; errors drop from percent-level to sub-percent on average. Ridge reconstructions for (c) an even ridge ($m = 1$) and (d) an odd ridge ($m = 2$): the teacher $\Phi_m(z)$ and learned student $I_m(z)$ are overlaid on $z \in [-1, 1]$, demonstrating correct parity and quantitative agreement of the calibrated polynomial.

an immediate engineering target. On the AOC, coherence management and spectral filtering merit systematic study when microLED illumination is used. From an algorithm-hardware co-design standpoint, integrating exact spin-elimination with native k -local optics promises compressed formulations that reduce variable count at fixed aperture, while KAN-based surrogates trained in situ open a path to hybrid optimization: learning workloads on one photonic substrate. Benchmarking against crystal-based four-body SPIMs and modern electronic annealers on representative k -SAT and higher-order inference tasks, and training optical KAN layers on scientific regression problems, will quantify the achievable speed, namely, energy advantages unlocked by structural nonlinearity.

In summary, the two-bounce relay turns structural nonlinearity into a massively parallel, per-window resource. In doing so, it closes a critical capability gap: it endows SLM-based optical systems with native, programmable k -local Ising dynamics and furnishes the independently tunable ridge functions needed for all-optical KANs, while preserving the simplicity, reconfigurability, and throughput that make diffractive photonics attractive for computation.

Taken together, our k -local Ising machine and optical KAN blocks constitute a single, reconfigurable photonic fabric that natively supports both discrete energy minimization and continuous function learning. Higher-order ($k > 2$) couplers encode structural constraints for combinatorial search, while KAN layers implement spline-like basis expansions and differentiable operators on the same optical primitives. This co-location marks a critical convergence point in optical computing: structure discovery (Ising) and parameterized modeling or surrogate physics (KAN) can be interleaved on-chip, share calibration and control, and amortize I/O and loss. Framed as one platform rather than two devices, the architecture reduces overhead, improves reuse of photonic components, and opens a path to field-programmable photonic co-processors that span discrete and continuous workloads.

ACKNOWLEDGEMENTS

N.G.B. acknowledges the support from the HORIZON EIC Pathfinder Challenges project HEISINGBERG (grant 101114978) and the EPSRC UK Multidisciplinary Centre for Neuromorphic Computing (grant UKRI982). Both authors thank the Weizmann-UK Make Connection grant (grant 142568) for support.

* n.g.berloff@damtp.cam.ac.uk

- [1] N. Mohseni, P. L. McMahon, and T. Byrnes, Ising machines as hardware solvers of combinatorial optimization problems, *Nature Reviews Physics* **4**, 363 (2022).
- [2] Y. Yamamoto, K. Aihara, T. Leleu, K.-i. Kawarabayashi, S. Kako, M. Fejer, K. Inoue, and H. Takesue, Coherent ising machines—optical neural networks operating at the quantum limit, *npj Quantum Information* **3**, 1 (2017).
- [3] T. Inagaki, Y. Haribara, K. Igarashi, T. Sonobe, S. Tamate, T. Honjo, A. Marandi, P. L. McMahon, T. Umeki, K. Enbutsu, *et al.*, A coherent ising machine for 2000-node optimization problems, *Science* **354**, 603 (2016).
- [4] P. L. McMahon, A. Marandi, Y. Haribara, R. Hamerly, C. Langrock, S. Tamate, T. Inagaki, H. Takesue, S. Utsunomiya, K. Aihara, *et al.*, A fully programmable 100-spin coherent ising machine with all-to-all connections, *Science* **354**, 614 (2016).
- [5] V. Pal, S. Mahler, C. Tradonsky, A. A. Friesem, and N. Davidson, Rapid fair sampling of the x y spin hamiltonian with a laser simulator, *Physical Review Research* **2**, 033008 (2020).
- [6] M. Babaeian, D. T. Nguyen, V. Demir, M. Akbulut, P.-A. Blanche, Y. Kaneda, S. Guha, M. A. Neifeld, and N. Peyghambarian, A single shot coherent ising machine based on a network of injection-locked multicore fiber lasers, *Nature communications* **10**, 1 (2019).
- [7] M. Parto, W. Hayenga, A. Marandi, D. N. Christodoulides, and M. Khajavikhan, Realizing

- spin hamiltonians in nanoscale active photonic lattices, *Nature materials* **19**, 725 (2020).
- [8] D. Pierangeli, G. Marcucci, and C. Conti, Large-scale photonic ising machine by spatial light modulation, *Physical review letters* **122**, 213902 (2019).
 - [9] N. G. Berloff, M. Silva, K. Kalinin, A. Askitopoulos, J. D. Töpfer, P. Cilibrizzi, W. Langbein, and P. G. Lagoudakis, Realizing the classical XY hamiltonian in polariton simulators, *Nature materials* (2017).
 - [10] K. P. Kalinin, A. Amo, J. Bloch, and N. G. Berloff, Polaritonic xy-ising machine, *Nanophotonics* **9**, 4127 (2020).
 - [11] M. Vretenar, B. Kassenberg, S. Bissesar, C. Toebes, and J. Klaers, Controllable josephson junction for photon bose-einstein condensates, *Physical Review Research* **3**, 023167 (2021).
 - [12] K. Kalinin, G. Mourgas-Alexandris, H. Ballani, N. G. Berloff, J. H. Clegg, D. Cletheroe, C. Gkantsidis, I. Haller, V. Lyutsarev, F. Parmigiani, L. Pickup, *et al.*, Analog iterative machine (aim): using light to solve quadratic optimization problems with mixed variables, *arXiv preprint arXiv:2304.12594* (2023).
 - [13] H. Goto, K. Endo, M. Suzuki, Y. Sakai, T. Kanao, Y. Hamakawa, R. Hidaka, M. Yamasaki, and K. Tatumura, High-performance combinatorial optimization based on classical mechanics, *Science Advances* **7**, eabe7953 (2021).
 - [14] K. Y. Camsari, R. Faria, B. M. Sutton, and S. Datta, Stochastic p-bits for invertible logic, *Physical Review X* **7**, 031014 (2017).
 - [15] K. Y. Camsari, B. M. Sutton, and S. Datta, P-bits for probabilistic spin logic, *Applied Physics Reviews* **6** (2019).
 - [16] D. Zhang, Z. Yuan, T. X. Hoang, W. Fu, C. E. Png, S. T. Lim, and A. Danner, All-optical scalable and programmable vcsel-based ising annealer with parallel feedback, *Optics Express* **33**, 22119 (2025).
 - [17] A. Lucas, Ising formulations of many np problems, *Frontiers in physics* **2**, 5 (2014).
 - [18] R. Monasson and R. Zecchina, Statistical mechanics of the random k-satisfiability model, *Physical Review E* **56**, 1357 (1997).
 - [19] M. Mézard, G. Parisi, and R. Zecchina, Analytic and algorithmic solution of random satisfiability problems, *Science* **297**, 812 (2002).
 - [20] M. Mézard, F. Ricci-Tersenghi, and R. Zecchina, Two solutions to diluted p-spin models and xorsat problems, *Journal of Statistical Physics* **111**, 505 (2003).
 - [21] J. Kempe, A. Kitaev, and O. Regev, The complexity of the local hamiltonian problem, *Siam journal on computing* **35**, 1070 (2006).
 - [22] G. Pedretti, F. Böhm, T. Bhattacharya, A. Heitmann, X. Zhang, M. Hizzani, G. Hutchinson, D. Kwon, J. Moon, E. Valiante, *et al.*, Solving boolean satisfiability problems with resistive content addressable memories, *npj Unconventional Computing* **2**, 7 (2025).
 - [23] E. Boros, Y. Crama, and E. Rodríguez-Heck, Compact quadratizations for pseudo-boolean functions, *Journal of combinatorial optimization* **39**, 687 (2020).
 - [24] E. Valiante, M. Hernandez, A. Barzegar, and H. G. Katzgraber, Computational overhead of locality reduction in binary optimization problems, *Computer Physics Communications* **269**, 108102 (2021).
 - [25] M. K. Bashar and N. Shukla, Designing ising machines with higher order spin interactions and their application in solving combinatorial optimization, *Scientific Reports* **13**, 9558 (2023).
 - [26] C. Bybee, D. Kleyko, D. E. Nikonov, A. Khosrowshahi, B. A. Olshausen, and F. T. Sommer, Efficient optimization with higher-order ising machines, *Nature Communications* **14**, 6033 (2023).
 - [27] N. G. Berloff, Exact spin elimination in ising hamiltonians and energy-based machine learning, *arXiv preprint arXiv:2505.07163* (2025).
 - [28] A. N. Kolmogorov, *On the representation of continuous functions of several variables by superpositions of continuous functions of a smaller number of variables* (American Mathematical Society, 1961).
 - [29] Z. Liu, Y. Wang, S. Vaidya, F. Ruehle, J. Halverson, M. Soljačić, T. Y. Hou, and M. Tegmark, Kan: Kolmogorov-arnold networks, *arXiv preprint arXiv:2404.19756* (2024).
 - [30] Y. Peng, S. Hooten, X. Yu, T. Van Vaerenbergh, Y. Yuan, X. Xiao, B. Tossoun, S. Cheung, M. Fiorentino, and R. Beausoleil, Photonic kan: a kolmogorov-arnold network inspired efficient photonic neuromorphic architecture, *arXiv preprint arXiv:2408.08407* (2024).
 - [31] ai1 Technologies LLC, Ai-driven credit decisioning and risk modeling with kolmogorov-arnold networks, <https://www.ai1.tech/> (2025), accessed: 22 August 2025.
 - [32] J. Sakellariou, A. Askitopoulos, G. Pastras, and S. I. Tsintzos, Encoding arbitrary ising hamiltonians on spatial photonic ising machines, *Physical Review Letters* **134**, 203801 (2025).
 - [33] D. Veraldi, D. Pierangeli, S. Gentilini, M. C. Strinati, J. Sakellariou, J. S. Cummins, A. Kamaletdinov, M. Syed, R. Z. Wang, N. G. Berloff, *et al.*, Fully programmable spatial photonic ising machine by focal plane division, *Physical Review Letters* **134**, 063802 (2025).
 - [34] R. Z. Wang, J. S. Cummins, M. Syed, N. Stroeve, G. Pastras, J. Sakellariou, S. Tsintzos, A. Askitopoulos, D. Veraldi, M. Calvanese Strinati, *et al.*, Efficient computation using spatial-photonic ising machines with low-rank and circulant matrix constraints, *Communications Physics* **8**, 86 (2025).
 - [35] B. Wu, W. Zhang, S. Zhang, H. Zhou, Z. Ruan, M. Li, D. Huang, J. Dong, and X. Zhang, A monolithically integrated optical ising machine, *Nature Communications* **16**, 4296 (2025).
 - [36] S. Kumar, H. Zhang, and Y.-P. Huang, Large-scale ising emulation with four body interaction and all-to-all connections, *Communications Physics* **3**, 108 (2020).
 - [37] T. Kanao and H. Goto, High-accuracy ising machine using kerr-nonlinear parametric oscillators with local four-body interactions, *npj Quantum Information* **7**, 18 (2021).
 - [38] C. C. Wanjura and F. Marquardt, Fully nonlinear neuromorphic computing with linear wave scattering, *Nature Physics* **20**, 1434 (2024).
 - [39] H. Wang, J. Hu, A. Morandi, A. Nardi, F. Xia, X. Li, R. Savo, Q. Liu, R. Grange, and S. Gigan, Large-scale photonic computing with nonlinear disordered media, *Nature Computational Science* **4**, 429 (2024).
 - [40] S. Bandyopadhyay, A. Sludds, S. Krastanov, R. Hamerly, N. Harris, D. Bunandar, M. Streshinsky, M. Hochberg, and D. Englund, Single chip photonic deep neural network with accelerated training, *arXiv preprint arXiv:2208.01623* (2022).

- [41] M. Yildirim, N. U. Dinc, I. Oguz, D. Psaltis, and C. Moser, Nonlinear processing with linear optics, *Nature Photonics* **18**, 1076 (2024).
- [42] N. Stroeve and N. G. Berloff, Discrete polynomial optimization with coherent networks of condensates and complex coupling switching, arXiv preprint arXiv:1910.00842 (2019).
- [43] L. N. Trefethen, *Approximation theory and approximation practice, extended edition* (SIAM, 2019).
- [44] R. Koekoek, P. A. Lesky, and R. F. Swarttouw, Hypergeometric orthogonal polynomials, in *Hypergeometric Orthogonal Polynomials and Their q -Analogues* (Springer, 2010) pp. 183–253.
- [45] S. Pai, Z. Sun, T. W. Hughes, T. Park, B. Bartlett, I. A. Williamson, M. Minkov, M. Milanizadeh, N. Abebe, F. Morichetti, *et al.*, Experimentally realized in situ backpropagation for deep learning in photonic neural networks, *Science* **380**, 398 (2023).
- [46] T. W. Hughes, M. Minkov, Y. Shi, and S. Fan, Training of photonic neural networks through in situ backpropagation and gradient measurement, *Optica* **5**, 864 (2018).
- [47] A. Momeni, B. Rahmani, B. Scellier, L. G. Wright, P. L. McMahon, C. C. Wanjura, Y. Li, A. Skalli, N. G. Berloff, T. Onodera, *et al.*, Training of physical neural networks, arXiv preprint arXiv:2406.03372 (2024).